# Pt-Calcium-Cobaltate Enables Sorption-Enhanced Steam Reforming of Glycerol Coupled with Chemical Looping $CH_4$ Combustion

Hanke Li,[1] Chengxiong Dang,[2] Yuhang Li,[2,3] Guangxing Yang,[1] Yonghai Cao,[1] Hongjuan Wang,[1] Feng Peng,[2] Hao Yu[1,*]

[1] *School of Chemistry and Chemical Engineering, Guangdong Provincial Key Lab of Green Chemical Product Technology, South China University of Technology, Guangzhou, 510641, China*

[2] *School of Chemistry and Chemical Engineering, Guangzhou University, Guangzhou 510006, China*

[3] *MOE Laboratory of Bioinorganic and Synthetic Chemistry, The Key Lab of Low-Carbon Chemistry and Energy Conservation of Guangdong Province, School of Chemistry, Sun Yat-sen University, Guangzhou 510275, China*

* Correspondence concerning this article should be addressed to Prof. Hao Yu (yuhao@scut.edu.cn)

**ABSTRACT**

As an efficient approach to high-purity hydrogen, the sorption-enhanced steam reforming (SESR) is usually highly energy-intensive. Herein, the sorbent decarbonation was conducted in the presence of $O_2$ to enable the exothermic reaction between CaO and cobalt oxides to form calcium cobaltate (CCO). By utilizing CCO as oxygen carrier (OC), the chemical looping methane combustion (CLMC) was employed prior to the SESR of glycerol (SESRG). The CCO was pre-reduced to generate a multi-functional material composed of metallic Co catalysts and CaO sorbent, which can significantly improve the $H_2$ yield from SESRG. With a simple Pt-doped CCO acting as pre-catalyst, $CO_2$ sorbent and OC, we realized 70% $CH_4$ conversion and 96 vol.% $H_2$ with 120% yield for 20 cycles. The promoting effects of Pt towards $CH_4$ conversion and $H_2$ production were rationalized by $CH_4$-TPR, XPS, SEM and TEM. Our results demonstrate the feasibility of process integration and intensification enabled by multi-functional materials.

**TOPICAL HEADING:** Reaction Engineering, Kinetics and Catalysis

**KEY WORDS**: Calcium cobaltate; Pt; hydrogen yield; Sorption-enhanced steam reforming of glycerol; Chemical looping methane combustion

# 1. INTRODUCTION

Enormous attention has been drawn either to renewable carbon-free power sources or to alleviating carbon emission in current industrial processes approaching to a decarbonized future. Hydrogen is deemed as an ideal environmentally benign energy carrier for its combustion only emits water.[1,2] However, nowadays over 90% of global hydrogen is still from fossil fuels,[3] thus making its production unsustainable from a long-term perspective. To address this issue, biomass-derived feedstocks have shown huge potential in recent decades for producing hydrogen because of its renewability, less energy consumption and milder reaction conditions compared with conventional methane steam reforming, petroleum refining, coal gasification or water electrolysis processes.[3] Glycerol as an abundant by-product from bio-diesel production has already been extensively studied for hydrogen production due to its broad availability, relatively high hydrogen content (57.1 at.% or 8.8 wt.%) and low toxicity.[4] So far, high-purity hydrogen (>96 vol.%) can be produced via steam reforming of glycerol combined with sorption-enhancement techniques.[5-9] As expressed in Eq. (1), the sorption-enhanced steam reforming of glycerol (SESRG) utilizes sorbent materials (such as CaO) to *in situ* remove $CO_2$ yielded from the reforming reaction, thereby shifting the equilibrium towards hydrogen production. The $CO_2$ fixed in the sorbent in the form of carbonates makes it convenient for further storage and utilization[10], allowing for a facile approach to carbon emission control.

$$C_3H_8O_3(g)+3H_2O(g)+3CaO(s)=7H_2(g)+3CaCO_3(s) \quad \Delta H_{r,298K} = -406 \text{ kJ/mol} \qquad (1)$$

However, to enable a long-term operation, calcination at high temperatures (~800 $^oC$) is usually required to commence the endothermic decomposition of $CaCO_3$ to decarbonate the

sorbent, thus making the overall process highly energy-intensive. Fortunately, it should be noted that the formation of calcium-transition-metal composite oxides (Ca-M-O, M=Co, Cu, Fe) via solid-state reactions between CaO and transition metal oxides may be more energetically favorable in the presence of oxygen.[11-13] Following this strategy, it has been demonstrated that calcium cobaltate (CCO) was feasible as a stable dual-functional material (SRG pre-catalyst and $CO_2$ sorbent) for SESRG for up to 120 reaction-decarbonation cycles.[14] As depicted in Figure S1a, the formation of $Ca_3Co_4O_9$ is exothermic within the calculated temperature range, thus consuming much less energy compared with the endothermic $CaCO_3$ decomposition. In addition, the Gibbs free energy changes of the formation of $Ca_3Co_4O_9$ depicted in Figure S1b are below zero within the calculated temperature range, in striking contrast with that of $CaCO_3$ decomposition which only goes below zero at $T$>827 ºC (1100 K). These advantages suggest that the energy efficiency of sorbent decarbonation could be dramatically improved if CCO material can be formed in the presence of $O_2$.

Unfortunately, the introduction of oxygen consumes $H_2$ produced in the next cycle of SESRG, thereby declining the overall $H_2$ yield. To overcome this, CCO reduction needs to be decoupled from SESRG to avoid $H_2$ consumption. It should be noted that CCO can be readily reduced to Co and CaO in hydrogen-rich atmosphere, implying that it can be applied as an oxygen carrier under certain circumstances, depending on the activity and mobility of its lattice oxygen. On the other hand, as $Ca_2Fe_2O_5$ has been reported as an efficient oxygen carrier for chemical looping methane combustion (CLMC) and Co is also an element in VIII group, [15,16] we proposed that CCO is a potential oxygen carrier (OC) that can be applied for a CLMC process. As an important clean fossil energy from shale gas, coalbed methane and methane hydrate,[17] CLMC

provides an efficient way to mitigate carbon emission. [18-20] It utilizes lattice oxygen from OC rather than air to oxidize methane to produce heat and energy, and a nearly pure $CO_2$ stream can be readily obtained for further capture and storage after condensation of steam, as expressed in Eq. (2) and Eq. (3),[21,22] where $M_xO_y$ stands for metal oxides.

$$\delta CH_4+M_xO_y \rightarrow \delta CO_2+2\delta H_2O+M_xO_{y-4\delta} \quad (2)$$

$$M_xO_{y-4\delta}+2\delta O_2 \rightarrow M_xO_y \quad (3)$$

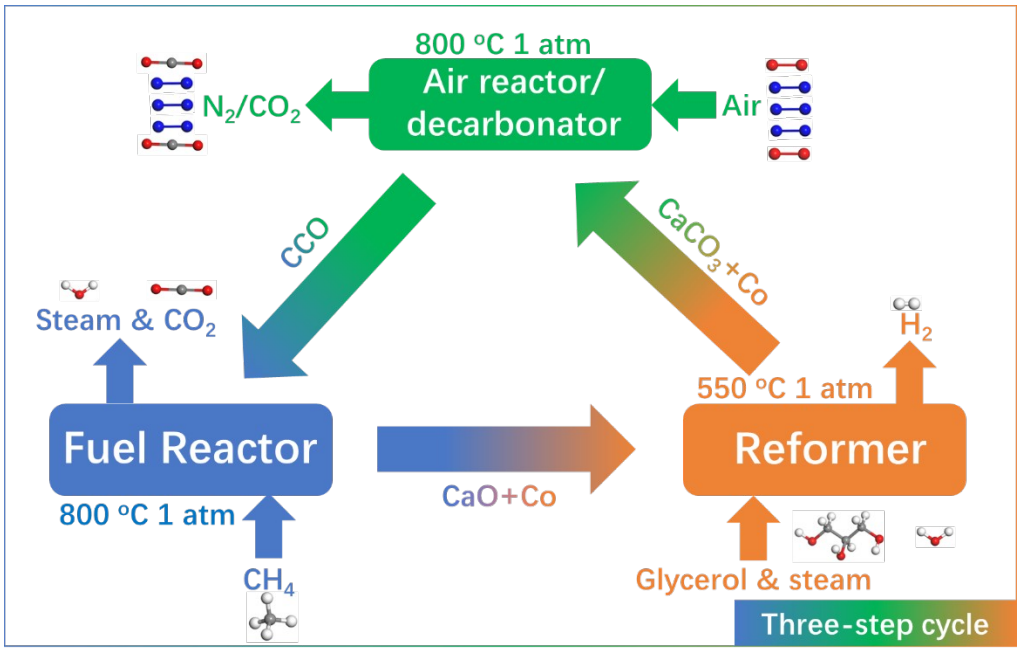


**Scheme 1** Illustration of the combination of SESRG for $H_2$ production and CLMC for Pt/CCO reduction.

CLMC: $Ca_3Co_4O_9(s)+1.5CH_4(g)=3CaO(s)+4Co(s)+1.5CO_2(g)+3H_2O(g)$ (4)

SESRG: $C_3H_8O_3(g)+3H_2O(g)+3CaO(s)=7H_2(g)+3CaCO_3(s)$ (5)

Regeneration: $3CaCO_3(s)+3O_2(g)+4Co(s)=Ca_3Co_4O_9(s)+3CO_2(g)$ (6)

Here, enlightened by the versatility exhibited by CCO acting as SRG pre-catalyst, $CO_2$ sorbent and OC, we demonstrated that energy-saving decarbonation and improved $H_2$ yield could be both achieved in a 3-step cycle composed of CLMC, SESRG and OC regeneration/sorbent

decarbonation using a Pt doped CCO material (Pt/CCO), in which Pt allowed for more effective methane activation and conversion in CLMC and more efficient $H_2$ production in SESRG. As illustrated in Scheme 1, $CH_4$ combustion was conducted upon Pt/CCO and it was reduced by $CH_4$ to generate the dual-functional material comprised of CaO, Co and Pt, which was subsequently subjected to SESRG to produce $H_2$ with >96% purity. Finally, the post-breakthrough dual-functional material is regenerated in air to release $CO_2$ and to form Pt/CCO. These steps are summarized by the reactions as Equation (4)-(6). In addition, the overall energy balance calculation suggested that the proposed 3-step process outperformed conventional 2-step SESRG-sorbent decarbonation in terms of overall energy and $CH_4$ consumption normalized to unit quantity of $H_2$ produced, as detailed in Scheme S1, Table S1, S2 and S3. It should be pointed out that introducing air in the sorbent decarbonation/oxygen carrier regeneration step makes it unable to obtain pure $CO_2$ stream. However, a $CO_2$-rich stream can still be produced, enabling various downstream applications, such as amine scrubbing $CO_2$ capture and chemical synthesis.[23,24] It is worth mentioning that Abanades, Anthony, Müller and co-workers have proposed 3-step Cu-Ca loops, wherein $CO_2$ capture, $H_2$ production and $CH_4$ combustion were also integrated in one cycle enabled by a CaO-CuO catalyst-sorbent-OC material.[25-27] It should be stressed that the 3-step cycle proposed here is quite different from the chemical looping – sorption enhanced steam reforming (CL-SESR) process reported by Dou, Chen and co-workers, since the CL-SESR process is essentially a 2-step cycle that utilizes heat produced by oxidation of metals to compensate energy input in the sorbent decarbonation step, thereby still resulting in $H_2$ consumption in the followed SESR step.[9,28] In this work, the recyclability of the Pt/CCO material was demonstrated for 20 cycles in the proposed 3-step loop with enhanced $H_2$ yield from SESRG and $CH_4$ conversion in

CLMC compared with CCO material without Pt doping, and the promoting effect of Pt was extensively investigated by multiple approaches to rationalize the evolution of the Pt/CCO material over the cycles.

# 2. EXPERIMENTAL

## 2.1 Chemicals

Chemicals involved in this work are used as received unless otherwise specified. Cobalt nitrate hexahydrate ($Co(NO_3)_2 \cdot 6H_2O$, 99.99% metal basis), calcium nitrate ($Ca(NO_3)_2 \cdot 4H_2O$, 99.98% metal basis) and chloroplatinic acid hexahydrate ($H_2PtCl_6 \cdot 6H_2O$, ACS regent, containing 37.5 wt.% Pt) were purchased from Shanghai Aladdin Biochemical Technology Co., Ltd. (Shanghai, China).

## 2.2 Synthesis of Pt/CCO

In a typical synthesis, aqueous solution containing equal molar ratio of $Ca^{2+}$ and $Co^{2+}$ was firstly prepared by dissolving 0.02 mol of corresponding nitrates in 50 mL deionized water, followed by adding the desired amount of $H_2PtCl_6$ aqueous solution (0.01 mol/L Pt) to achieve 1 wt.% Pt content in the Pt/CCO material. After vigorous agitation for 30 min at room temperature, the solution was dried at 120 $^{o}$C overnight to obtain precursors, followed by calcination at 800 $^{o}$C for 4 h in air to obtain fresh Pt/CCO material. The Pt content of the as-prepared Pt/CCO material was determined to be 1.07 wt.% by a PerkinElmer OPTIMA 7300 DV inductively coupled plasma – optical emission spectrometer, as detailed in Supplementary Text. The CCO material for reference purposes was synthesized using the identical procedure without adding $H_2PtCl_6$ aqueous solution.

**2.3 Characterizations of Pt/CCO**

X-ray diffraction (XRD) patterns were recorded on a PANalytical X'Pert powder diffractometer with monochromatic Cu K$\alpha$ radiation ($\lambda$=0.15406 nm) at 12°/min scan rate and 0.02° step size to determine the crystal phase of the materials. The generator voltage and tube current were at 40 kV and 40 mA, respectively. The diffraction peaks were matched using the International Center for Diffraction Data (ICDD) database.

The specific surface area of Pt/CCO was determined by the Brunauer–Emmett–Teller (BET) method using $N_2$ physisorption at 77 K (-196 $^oC$) by a Micromeritics ASAP 2010 apparatus. The samples were degassed at 150 $^oC$ for 6 h prior to the measurement.

The surface morphology and microstructure of fresh and spent Pt/CCO were characterized by a Zeiss Merlin field emission scanning electron microscope (FESEM) operated at 5.0 kV. Transmission electron microscopy (TEM) images, high-angle annular dark field - scanning TEM (HAADF-STEM) images, high resolution TEM (HRTEM) images and energy dispersive X-ray spectroscopic (EDS) element maps were recorded on a JEOL JEM-2100F field emission transmission electron microscope operated at 200 kV. Specimens for TEM were prepared by ultrasonically dispersing the sample in ethanol, followed by depositing a drop of the suspension onto a copper microgrid covered with amorphous carbon.

X-ray photoelectron spectroscopy (XPS) analysis of Pt/CCO was carried out with a ThermoFisher ESCALAB 250Xi spectrometer using monochromatic Al K$\alpha$ (1486.6 eV) radiation. High resolution XPS spectra of Co 2p, Ca 2p, Pt 4f along with C 1s and O 1s were recorded. The binding energies were referenced to the adventitious C 1s peak at 284.8 eV. The obtained XPS spectra was deconvoluted and fitted using the XPSPEAK 41 software with a Shirley-type

background and 20% Gaussian-Lorentz factor. The XPS spectra of Pt 4f were not fitted or deconvoluted due to their low signal to noise ratio.

$H_2$ temperature programmed reduction ($H_2$-TPR) experiments were performed on a Xianquan TP-5080 apparatus equipped with a thermal conductivity detector (TCD). Typically, 50 mg of sample was firstly pretreated in $N_2$ (30 $cm^3$/min) at 200 °C for 0.5 h. After cooling it to room temperature, 10 vol.% $H_2/N_2$ (30 $cm^3$/min) was used to reduce the sample from 30 °C to 800 °C at a temperature ramping rate of 10 °C/min. For samples after $CH_4$ combustion and SESRG, they were firstly treated in $N_2$ at 700 °C for 0.5 h to desorb $CO_2$. The quantitative analysis was performed to determine the oxygen carrying capacity, by using CuO powder (99.99% metal basis) as reference to calibrate the TCD signal.

$CH_4$ temperature programmed reduction ($CH_4$-TPR) experiments were performed on the Xianquan TP-5080 apparatus connected to a HIDEN QIC-20 mass spectrometer (MS) equipped with an electron impact ion source operated at 70 eV. Typically, 50 mg of sample was firstly pretreated in He (30 $cm^3$/min) at 200 °C for 0.5 h. After cooling it to room temperature, 10 vol.% $CH_4$/He (30 $cm^3$/min) was used to reduce the sample with the temperature ramping from 30 °C to 800 °C at a heating rate of 10 °C/min and holding at 800 °C for 60 min. The MS was operated in selected ion monitoring (SIM) mode, by which characteristic ions of $H_2$ (*m/z*=2), $CH_4$ (*m/z*=15), CO (*m/z*=28) and $CO_2$ (*m/z*=44) were monitored concurrently. The off-gas from TCD was introduced into the capillary sampling tube of the MS so as to detect $H_2$, $CH_4$, CO and $CO_2$.

**2.4 Performance tests**

The performance tests of the Pt/CCO were performed in a quartz tubular fixed bed reactor with an inner diameter of 9.6 mm and a length of 330 mm. The temperature of catalyst bed was

monitored by a K-type thermocouple with a diameter of 3 mm. The schematic diagram of the experiment set-up used for the performance test are given in Figure S2. In a typical experiment, 1.0 g Pt/CCO was mounted into the reactor and heated to 800 °C in 50 $Ncm^3$/min (standard milliliter per minute, the same below) $N_2$, then 30% $CH_4/N_2$ (50 $Ncm^3$/min) was introduced to the reactor to start the $CH_4$ combustion for 14 min (the duration is chosen based on the results in Figure 4b). Thereafter, the reactor was purged with 100 $Ncm^3$/min $N_2$ then cooled down to 550 °C. A mixture of glycerol and water (Steam/Carbon=4) was fed into the upper part of the catalyst bed using a syringe pump through a stainless-steel capillary tube (0.3 mm I.D.) at 0.02 mL/min in the presence of 30 $Ncm^3$/min $N_2$ flow (GHSV=1309 $h^{-1}$) to start the SESRG reaction for 20 min (the duration is chosen based on the results in Figure S8). Then, the reactor was heated to 800 °C and kept for 30 min (the duration is chosen based on our previous work [14]) with 21 vol.% $O_2/N_2$ (30 $Ncm^3$/min) to regenerate Pt/CCO. And the reactor was purged with 100 $Ncm^3$/min $N_2$ for 10 min after each cycle. The mole fractions of $H_2$, CO, $CH_4$ and $CO_2$ in the off-gas were monitored by a GC9790 online gas chromatograph (GC) equipped with a TDX-1 packed column, a methanator, a TCD and a flame ionization detector (FID).

For $CH_4$ combustion, the $CH_4$ conversion ( $X_{CH_4}$ ) and $CO_2$ selectivity ( $S_{CO_2}$ ) are calculated by the following equations

$$X_{CH_4} = \frac{c_{CH_4,in} - c_{CH_4,out}}{c_{CH_4,in}}$$

$$S_{CO_2} = \frac{c_{CO_2,out}}{c_{CH_4,in} - c_{CH_4,out}}$$

For SESRG reactions, the dry basis $N_2$-free mole fractions of gaseous products ( $c_i$, $i$=$H_2$,

$CH_4$, CO or $CO_2$) and the hydrogen yield ( $Y_{H_2}$ ) are calculated by the following equations

$$c_i = \frac{c_{i,out}}{c_{H_2,out} + c_{CH_4,out} + c_{CO,out} + c_{CO_2,out}} \times 100\%$$

$$Y_{H_2} = \frac{n_{H_2}}{7n_{glycerol}} \times 100\%$$

### 2.5 Thermodynamic and overall energy balance calculation

Thermodynamic calculations were carried out to compare the enthalpy change and Gibbs free energy change of CCO formation and $CaCO_3$ decomposition, wherein $Ca_3Co_4O_9$ was used to represent CCO, see Figure S1 for more details. Quantitative analysis of the dry-basis $N_2$ free mole fractions of $H_2$ and $CO_2$ at the thermodynamic equilibrium for pre-breakthrough and post-breakthrough stages of SESRG was performed using ASPEN Plus V10 software by minimizing the Gibbs free energy, detailed descriptions of the method and associated results could be found in Supplementary material, Table S7 and Table S8. The overall energy balance calculation was performed to demonstrate the energy-saving feature of proposed CLMC-SESRG-OC regeneration/ sorbent decarbonation cycle, compared with conventional SESRG-sorbent decarbonation cycle. The calculation method and associated results are detailed in Supplementary Text, Scheme S1, Table S1, Table S2 and Table S3.

## 3. RESULTS AND DISCUSSION

### 3.1 Characterizations of the Pt/CCO multi-functional material

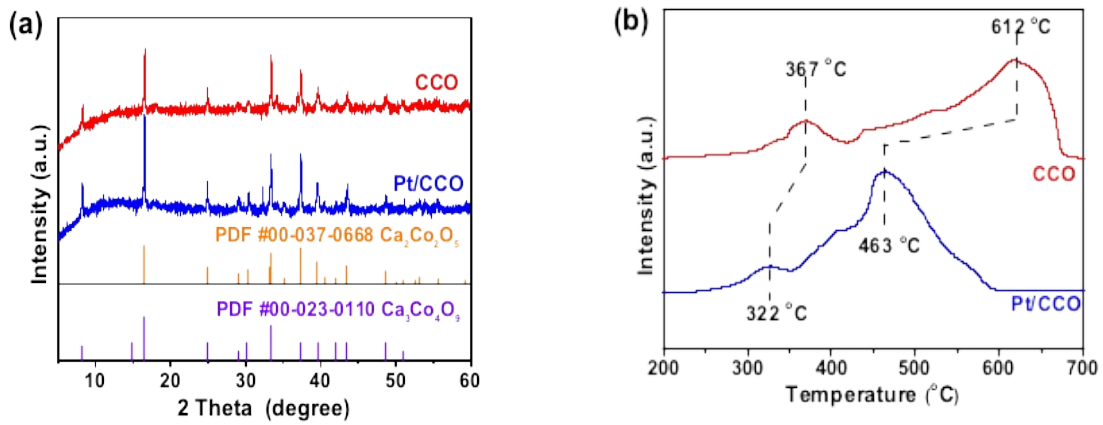


**Figure 1** (a) The XRD pattern and (b) $H_2$-TPR profile with CCO as reference of the as-synthesized Pt/CCO multi-functional material.

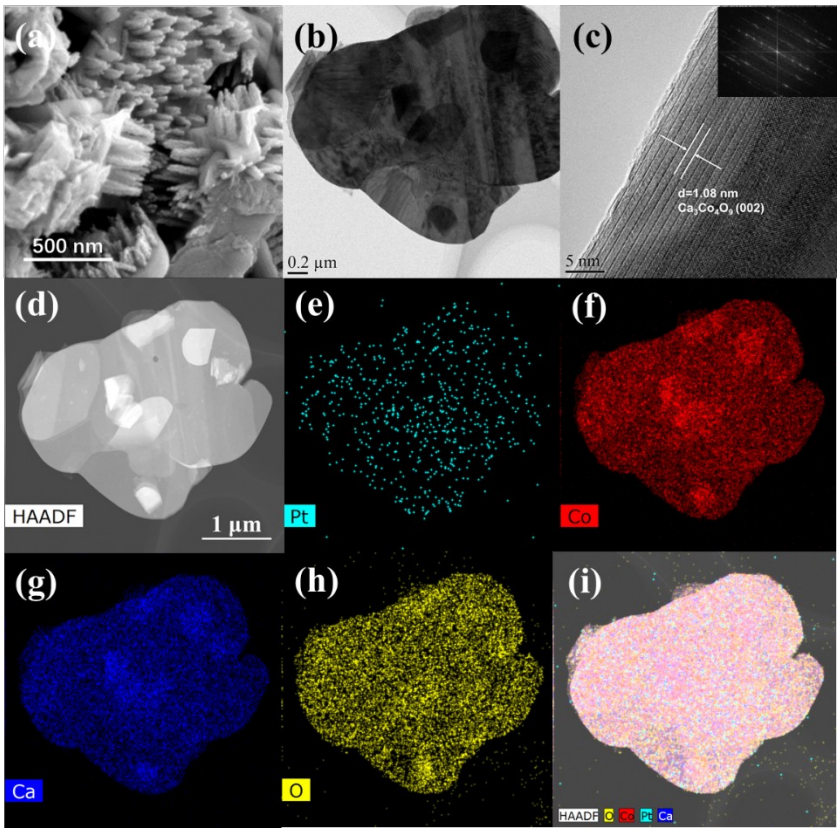


**Figure 2** (a) FESEM image, (b) TEM image, (c) HRTEM image (inset shows the FFT pattern of the image), (d)~(h) HAADF-STEM image and corresponding EDS element maps of Pt, Co, Ca

and O (scale bar: 1 μm), (i) overlaps of (d)~(h) of the fresh Pt/CCO multi-functional material.

Noble metals are expected to improve the activation of methane and also the $H_2$ production in steam reforming of glycerol.[29-35] A preliminary screening of M/CCO (M=Pt, Pd, Rh, Ru, Ir) materials in terms of $H_2$ production via SESRG and $CH_4$ conversion revealed that Pt outperformed other noble metals, as illustrated in Figure S3. Hence, Pt/CCO was applied for further investigation. As shown in Figure 1a and Figure S4a, the formation of CCO phases in Pt/CCO can be verified by the characteristic reflections at 16.5°, 33.3°, 37.2°, 39.5°, etc., probably in the stoichiometry of $Ca_2Co_2O_5$, $Ca_3Co_4O_9$ or $Ca_9Co_{12}O_{33}$, suggesting that the CCO phase can be preserved after Pt doping. Huang and co-workers reported the expansion of (002) facet when 3.7~7.2 wt.% Pt was doped into $Ca_3Co_4O_9$.[36] However, the expansion can be hardly observed due to the very low content of Pt of 1 wt.% in this work. On the other hand, trace $Co_3O_4$ phase could also be identified due to the incomplete solid-state reactions between CaO and Co species at 800 $^oC$, as depicted in Figure S4b. The HRTEM image depicted in Figure 2c and Figure S5e-h further confirmed the formation of misfit-layered $Co_3Co_4O_9$ with the characteristic 1.08 nm interval between adjacent [$CoO_2$] sublattices along the *c*-axis. [37,38] On the other hand, neither metallic Pt nor Pt oxides were identified in the XRD patterns (Figure 1a and Figure S4a) or observed in TEM (Figure 2b) and HAADF-STEM (Figure 2d) images. The uniform distribution of Pt with Co, Ca and O in the EDS elemental maps (Figure 2e-i & Figure S5a-d) suggests the doping of Pt into the bulk CCO phase. In addition, the hierarchical structure with some nanorods on the bulk flake can be observed in the FESEM image (Figure 2a) regardless of Pt doping, and the structure provided more available solid-gas interfaces, thereby being more favorable for reactant conversion.[14]

Furthermore, Pt-doping dramatically enhanced the reducibility of CCO. As shown in Figure 1b, the $H_2$ consumption peaks from the reduction of bulk CCO phase and surface $Co_3O_4$ species are downshifted by 169 °C and 45 °C, respectively, probably owing to the superior $H_2$ activation on Pt.[39,40] It is also noted that the peak located at 322 °C (367 °C for CCO) is much smaller compared to the peak located at 463 °C (612 °C for CCO), suggesting surface $Co_3O_4$ is reduced prior to CCO species. The BET specific surface area of the as-prepared Pt/CCO was 6.0 $m^2/g$ (see Figure S6 for the isotherm), which could be rationalized by the fact that it was prepared by calcination at 800 °C.

To probe the chemical states of the as-prepared Pt/CCO, we preformed XPS analysis on core-level Co 2p, Ca 2p and Pt 4f spectra. As depicted in Figure S7a, the Co 2p XPS spectrum could be deconvoluted to two sets of doublets, corresponding to Co(IV) and Co(III), again confirming the existence of CCO species featured by altered $[CoO_2]$ and $[Ca_{0.5}CoO_2]$ sublattices. As it presents an average oxidation state higher than +3, Co atoms in the layer-structured CCO species are more electron-donating compared to common cobalt oxides (e.g. CoO, $Co_3O_4$, $Co_2O_3$).[41] The Ca 2p XPS spectrum (Figure S7b) could also be deconvoluted to two sets of doublets, corresponding to Ca(II) coordinated to Co at different chemical valence in $[Ca_{0.5}CoO_2]$ sublattices.[41] As shown in Figure S7c, a set of distinguishable doublets located at *ca*. 74.0 eV and *ca*. 77.3 eV suggested the existence of Pt(IV) species, [42,43] due to the substitution of Co by Pt atoms in the CCO lattice via solid-state reactions between CCO and Pt oxides. With the structural and morphological properties of Pt/CCO multi-functional material being clarified, we therefore subjected it to the proposed CLMC-SESRG-OC regeneration/sorbent decarbonation cycles.

### 3.2 Performance of Pt/CCO in SESRG

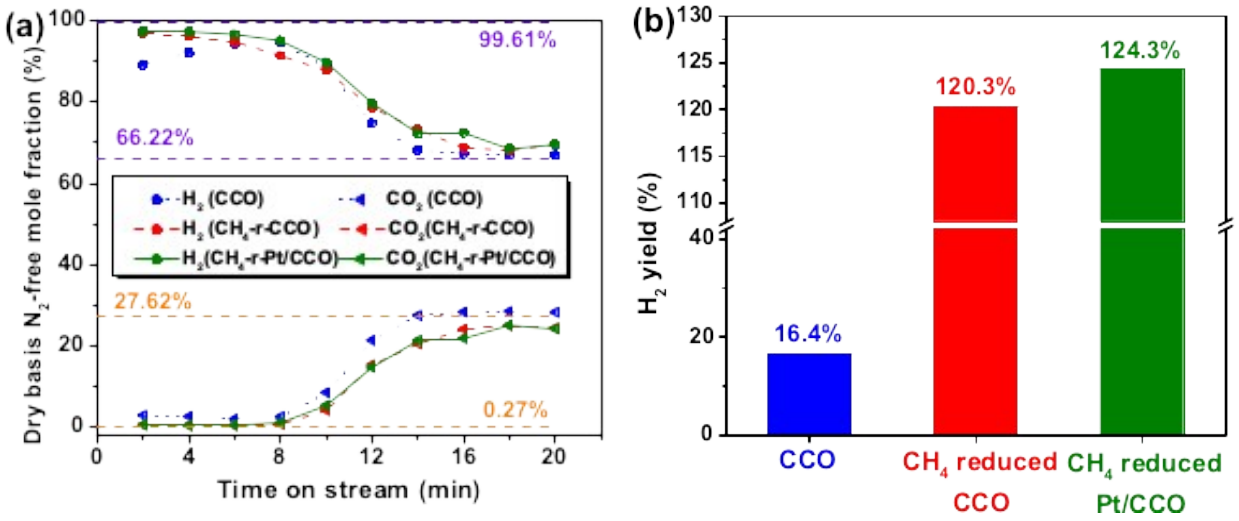


**Figure 3** (a) Typical dry basis $N_2$-free gaseous product evolution profile of SESRG, the horizontal dashed lines represent mole fractions of $H_2$ (violet) and $CO_2$ (orange) at thermodynamic equilibrium at the pre-breakthrough and post-breakthrough stages, respectively, (b) $H_2$ yield over CCO, $CH_4$-reduced CCO and $CH_4$-reduced Pt/CCO materials in SESRG measured by online GC. Reaction conditions for $CH_4$ reduction: 101.325 kPa, 800 °C, 50 $Ncm^3$/min $CH_4$(30 vol.%)/$N_2$, 1 g CCO or Pt/CCO, 14 min; reaction conditions for SESRG: 101.325 kPa, 550 °C, S/C=4, 0.02 mL/min, 30 $Ncm^3$/min $N_2$ (GHSV=1309 $h^{-1}$), 1 g CCO or Pt/CCO, 20 min.

The evolution of mole fractions of dry-basis $N_2$-free gaseous products in a typical SESRG reaction over the $CH_4$-reduced Pt/CCO material presents three characteristic stages composed of pre-breakthrough, breakthrough and post-breakthrough (see Figure S8).[44,45] In the pre-breakthrough stage, 96.0% $H_2$ can be produced with only 0.7% $CO_2$ emission, demonstrating a remarkable sorption-enhancement effect by *in situ* $CO_2$ capture compared with 69.5% $H_2$ and 24.0% $CO_2$ in the post-breakthrough stage. It was noted in Figure 3a that the enhancement of $H_2$ mole fraction for $CH_4$ reduced CCO and Pt/CCO mainly occurred in the beginning of the pre-breakthrough stage, suggesting CCO consumed $H_2$ as soon as the SESRG reaction began. After

pre-reduction by $CH_4$, $H_2$ mole fraction was slightly lower than the thermodynamic equilibrium value at the pre-breakthrough stage, possibly due to consumption by reverse water gas shift reaction (see Table S7 and S8 for details), whereas $CO_2$ mole fraction was quite close to its equilibrium value. More importantly, the pre-reduction by $CH_4$ improved the $H_2$ mole fraction and $H_2$ yield of CCO by 4 percentage points and 6.3 times, respectively, as shown in Figure 3b and Table S4, demonstrating the $CH_4$ reduction can compensate for the $H_2$ consumption by the oxides in SESRG step. Moreover, $H_2$ mole fraction and yield were further enhanced by doping CCO with Pt, suggesting the promoting effect of Pt towards $H_2$ production. It was noticed that the $H_2$ yield exceeded 100% over the $CH_4$-reduced CCO and Pt/CCO. The excess $H_2$ was probably contributed by the reforming/gasification of coke deposited during the $CH_4$ combustion (see section 3.4). To better verify the promoting effect, SESRG tests were also conducted on the $H_2$-reduced CCO and Pt/CCO materials. As shown in Table S5, $H_2$-reduced Pt/CCO gave both higher $H_2$ mole fraction and $H_2$ yield compared with $H_2$-reduced CCO, i.e. 96.9% vs. 95.3% and 87.9% vs. 84.2%, accompanied by the lower CO mole fraction, i.e. 1.5% vs. 2.7%, suggesting that Pt promotes SESRG possibly by facilitating water-gas shift reaction (WGSR).[46]

### 3.3 Performance of Pt/CCO in CLMC

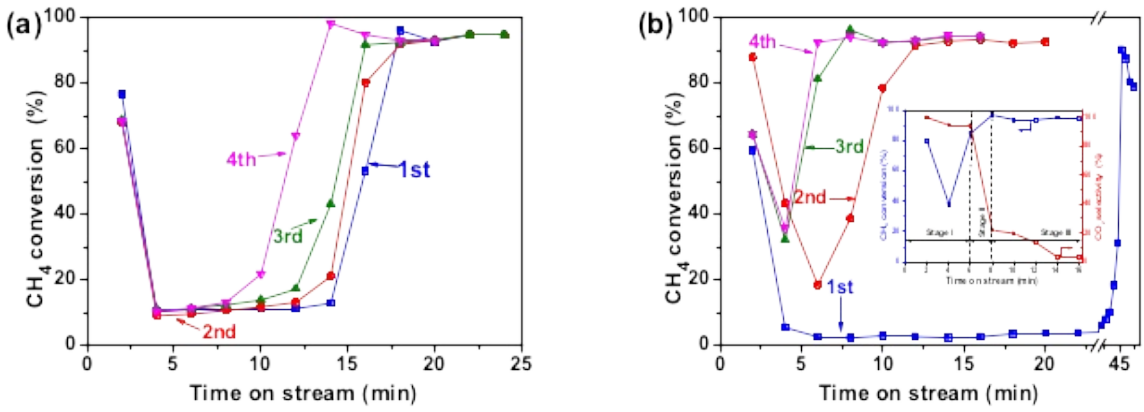

**Figure 4** Evolutions of $CH_4$ conversion during the $CH_4$ combustion step for four cyclic CLMC-SESRG-OC regeneration/sorbent decarbonation tests over (a) CCO and (b) Pt/CCO (The inset demonstrates the evolution of $CH_4$ conversion along with $CO_2$ selectivity over the $CH_4$-reduced Pt/CCO in the 3rd cycle). Reaction conditions for CLMC: 101.325 kPa, 800 °C, 50 $Ncm^3$/min $CH_4$(30 vol.%)/$N_2$, 1 g CCO or Pt/CCO, 14 min; reaction conditions for SESRG: 101.325 kPa, 550 °C, S/C=4, 0.02 $cm^3$/min, 30 $Ncm^3$/min $N_2$, 1 g CCO or Pt/CCO, 20 min; OC regeneration/sorbent decarbonation conditions: 101.325 kPa, 800 °C, 30 $Ncm^3$/min $O_2$(21 vol.%)/$N_2$, 30 min.

Figure 4 shows the promoting effect of Pt on $CH_4$ conversion. When the fresh CCO or Pt/CCO materials was subjected to the $CH_4$ combustion, a sharp decline of $CH_4$ conversion followed by a low-$CH_4$-conversion period was observed, although the initial $CH_4$ conversion can be high up to ~80%. After that, almost complete $CH_4$ conversion can be reached. The period with low $CH_4$ conversions can be observed even after four cycles over CCO. The longer period may result in severe sintering of CaO and Co at 800 °C, thereby deteriorating both $CO_2$ capture capacity and glycerol reforming activity in the subsequent SESRG step, which were identified after shutting down the $CH_4$ reduction reaction in the low-$CH_4$-conversion period, as depicted in Figure S9. It was observed that the Pt-doping significantly shortened the period with low $CH_4$ conversions, despite the long-standing period in the 1st cycle. From the 3rd cycle on, it took less than 8 min to achieve the complete conversion of $CH_4$. The inset in Figure 4b depicts the evolution of $CH_4$ conversion along with $CO_2$ selectivity for the 3rd cycle over Pt/CCO, wherein three stages can be clearly distinguished. Stage I was featured by the relatively high $CH_4$ conversion and over 90% $CO_2$ selectivity, suggesting $CH_4$ was converted largely in the way of complete oxidation. With the oxygen being consumed in Pt/CCO, the reaction proceeded to stage II, wherein the

partial oxidation and pyrolysis of $CH_4$ took place, featured by descending $CO_2$ selectivity and ascending $CH_4$ conversion. When the oxygen in Pt/CCO was finally depleted, the reaction entered stage III, wherein the high $CH_4$ conversion and low $CO_2$ selectivity were a result of $CH_4$ pyrolysis catalyzed by metallic Co and Pt as detailed later. To sum up, the incorporation of Pt into CCO significantly promoted the $CH_4$ conversion.

### 3.4 Recyclability of the coupled CLMC-SESRG process

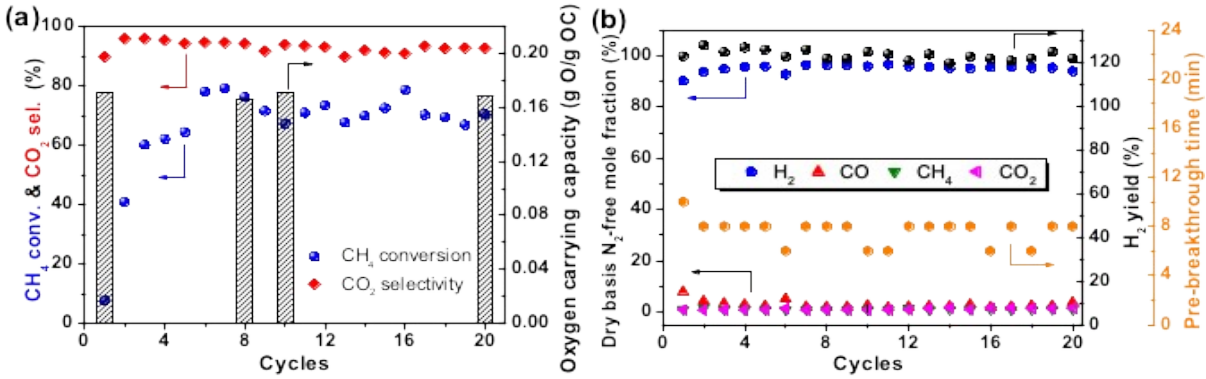


**Figure 5** Evolutions of (a) $CH_4$ conversion, $CO_2$ selectivity and oxygen carrying capacity for $CH_4$ combustion, and (b) dry basis $N_2$-free mole fraction of gaseous products, $H_2$ yield and pre-breakthrough time in SESRG step during 20 CLMC-SESRG-OC regeneration/sorbent decarbonation cycles. "Breakthrough" is defined as the point when dry basis $N_2$-free mole fraction of $CO_2$ exceeds 3%, and pre-breakthrough time is the duration when dry basis $N_2$-free mole fraction of $CO_2$ is below 3%. Reaction conditions for CLMC: 101.325 kPa, 800 °C, 50 $Ncm^3$/min $CH_4$(30 vol.%)/$N_2$, 1 g Pt/CCO, 14 min; reaction conditions for SESRG: 101.325 kPa, 550 °C, S/C=4, 0.02 mL/min, 30 $Ncm^3$/min $N_2$ (GHSV=1309 $h^{-1}$), 1 g Pt/CCO, 20 min; OC regeneration/sorbent decarbonation conditions: 101.325 kPa, 800 °C, 30 $Ncm^3$/min $O_2$(21 vol.%)/ $N_2$, 30 min.

To test the feasibility of the Pt/CCO in the proposed CLMC-SESRG-OC regeneration/sorbent decarbonation cycle, we performed a stability test for 20 cycles. As shown in Figure 5a, the average $CH_4$ conversion during Stage I significantly ascended from 7.8% to 78.1% after the first 6 cycles, implying the evolution of catalyst during the cycling test (see sub-section 3.5 for explanation), then stabilized at around 70% with over 90% $CO_2$ selectivity during the following 14 cycles, suggesting good stability in terms of CLMC. The oxygen carrying capacity of cycled Pt/CCO calculated from the quantitative $H_2$-TPR analysis (as detailed in Figure S10 and Table S6) retained at around 0.17 g O/g OC, demonstrating the excellent stability of Pt/CCO acting as OC. Meanwhile, Pt/CCO also displayed excellent stability towards SESRG. As shown in Figure 5b, the average $H_2$ mole fraction during the pre-breakthrough stage increased from 90.2 % to 95.0 % after the first 3 cycles and then stabilized at around 96% in the following 17 cycles. The $H_2$ yield in the pre-breakthrough stage maintained at around 120%. According to Dou et al., $H_2$ yield in SRG reaction should be close to 100% with S/C ratio higher than 3 at above 500 $^oC$.[47] In our case, the excess hydrogen can be rationalized by the reaction $C + H_2O \rightleftharpoons CO + H_2$ followed by WGSR at high S/C ratios, in which the coke was from $CH_4$ pyrolysis. The carbon formation was initially observed at the beginning of stage II of $CH_4$ combustion step according to the carbon balance. As shown in Figure S11, the carbon balance dropped from ~100% to 84% at the beginning of stage II, suggesting that carbon generated from $CH_4$ decomposition started to deposit on the catalyst. At the meantime, CO and $CO_2$ were both detected in stage II, indicating that CoO must have been reduced to Co. Thus, it is reasonable to conclude a metallic cobalt catalyzed the coke formation.

As an essential descriptor, pre-breakthrough time demonstrates the SE effect provided by the $CO_2$ sorbent. And more specifically, the evolution of pre-breakthrough time over cycles reflects

the recyclability of the sorbent. In this work, an average pre-breakthrough time of 7.5 min was achieved for 20 cycles. Moreover, there were no noticeable changes of other gaseous products after the 4$^{th}$ cycle as well. In summary, the proposed CLMC-SESRG-OC regeneration/sorbent decarbonation process is feasible and stable for 20 cycles using a simple Pt/CCO multi-functional material.

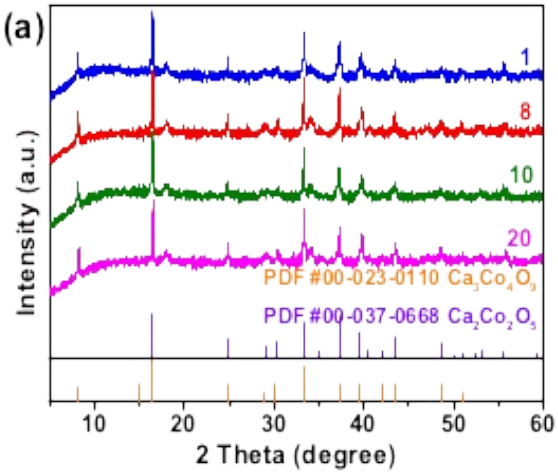


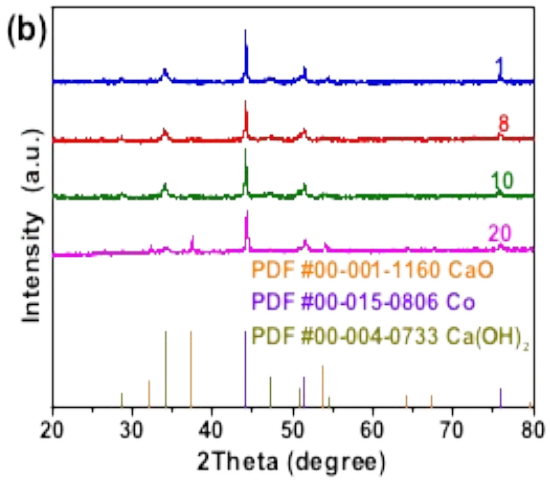

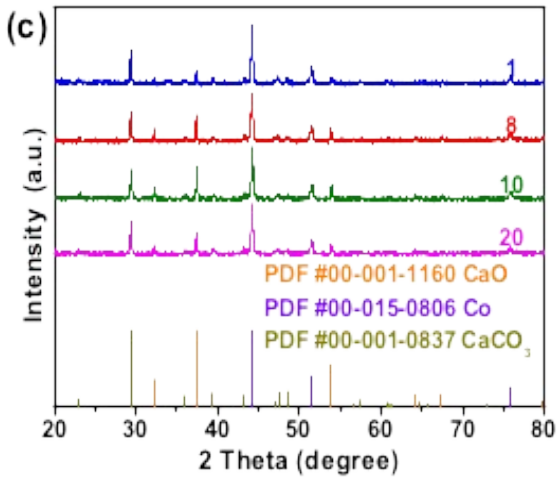


**Figure 6** XRD patterns of Pt/CCO after (a) OC regeneration/sorbent decarbonation, (b) $CH_4$ combustion and (c) SESRG steps, respectively, after 1st, 8th, 10th and 20th cycle.

XRD and $H_2$-TPR were performed to clarify the phase change in the repeated CLMC-SESRG-OC regeneration/sorbent decarbonation cycles. As shown in Figure 6a, CCO phases can still be preserved after multiple cycles, as observed in the fresh Pt/CCO. By subjecting Pt/CCO to $CH_4$ combustion, it is reduced to CaO and metallic Co, as depicted in Figure 6b. The appearance of $Ca(OH)_2$ phase was resulted from the hydration of CaO while exposed to moisture in the air.[48-50] In the following SESRG step, CaO is carbonated to $CaCO_3$, as evidenced by the emergence of reflections at 29.5°, 39.4°, 47.5° and 48.5° in Figure 6c. It was observed that CaO suffered from sintering during the repeated CLMC-SESRG-OC regeneration/sorbent decarbonation cycles, possibly owing to $CH_4$ combustion being carried out at 800 °C.[51] Nevertheless, this had little effect on the stability since CaO underwent the solid-state reaction with $Co_3O_4$ to form CCO in the following OC regeneration/sorbent decarbonation step, thus guaranteeing the controllable CaO

sintering. At this point, we can conclude the major phase changes in $CH_4$ combustion, SESRG and OC regeneration/sorbent decarbonation, respectively, as expressed in Eq. (4) – Eq. (6), in which $Ca_3Co_4O_9$ is used to represent CCO. And as these phase changes occur in the 1st, 8th, 10th and 20th cycle repeatedly, it is fair to suggest that they behave in a highly reversible manner throughout 20 cycles.

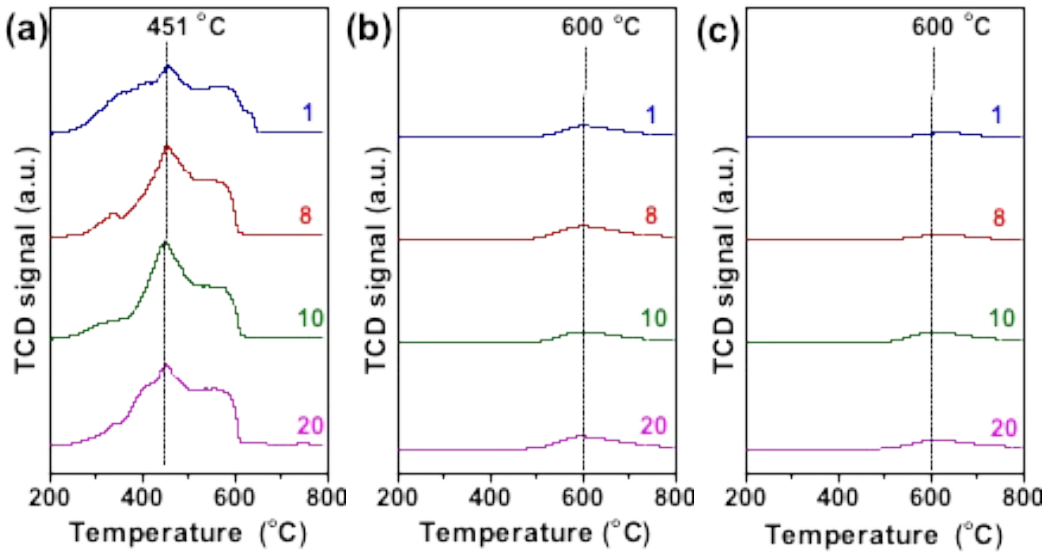


**Figure 7** $H_2$-TPR profiles of Pt/CCO after (a) OC regeneration/sorbent decarbonation, (b) $CH_4$ combustion and (c) SESRG steps, respectively, after 1st, 8th, 10th and 20th cycle.

The reduction behaviors of CCO and Pt/CCO may help us to probe the role of Pt in promoting reducibility of CCO. As shown in Figure 7a, the spent Pt/CCO after multiple cycles shows two distinguishable sets of peaks in the $H_2$-TPR profiles as observed in the fresh Pt/CCO, indicating that the phase change between CCO and Ca/Co species is highly reversible. The peak corresponding to bulk CCO phase reduction after cycles shifts to the lower temperature by 12 °C (463 °C→451 °C) compared to the fresh pre-catalyst in Figure 1b, implying the improved ability

for hydrogen activation. After the $CH_4$ combustion step, only a small peak can be observed at 600 °C, as illustrated in Figure 7b. It could be attributed to the methanation of polymeric coke originated from $CH_4$ pyrolysis.[52] In the following SESRG step, part of the coke would be gasified by steam as evidenced by the decrease of peak area at 600 °C in Figure 7c. In addition, the absence of peaks corresponding to the reduction of $CoO_x$ and CCO in Figure 7b and Figure 7(c) also suggests the complete reduction of Pt/CCO in the $CH_4$ combustion step, thereby guaranteeing the high $H_2$ yield in the following SESRG step.

### 3.5 Promoting effect of Pt

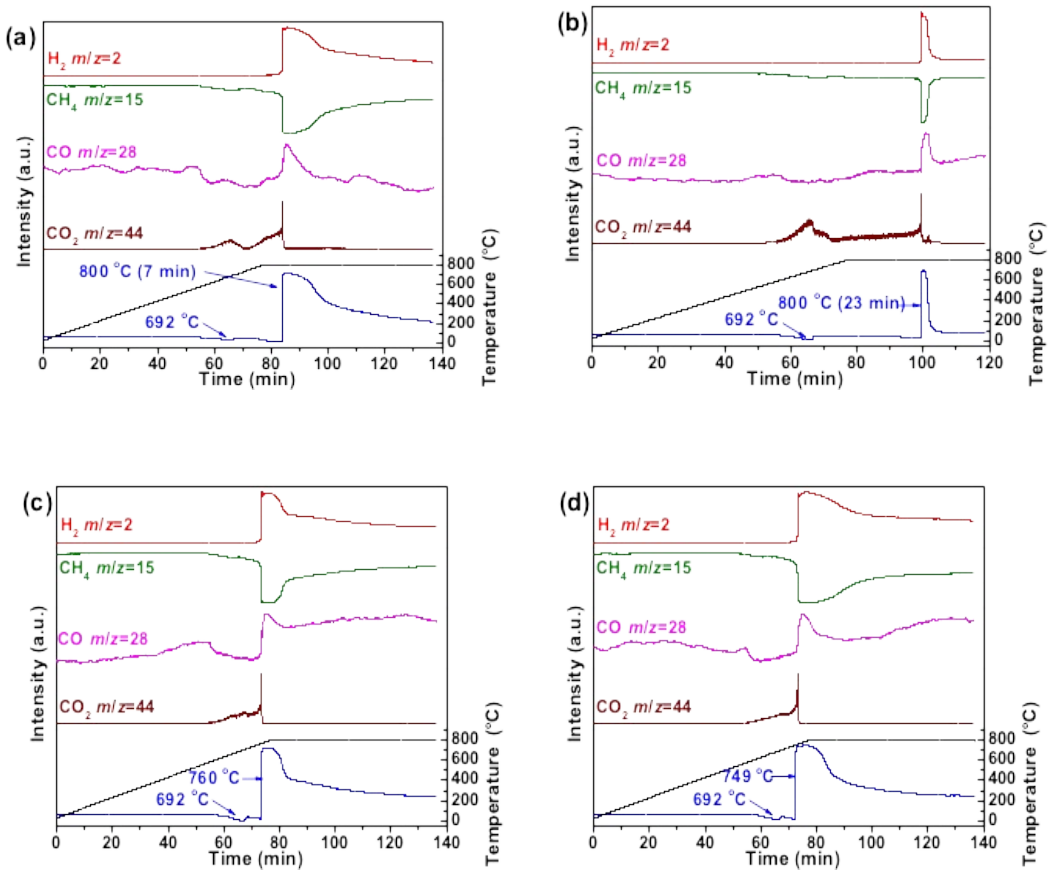

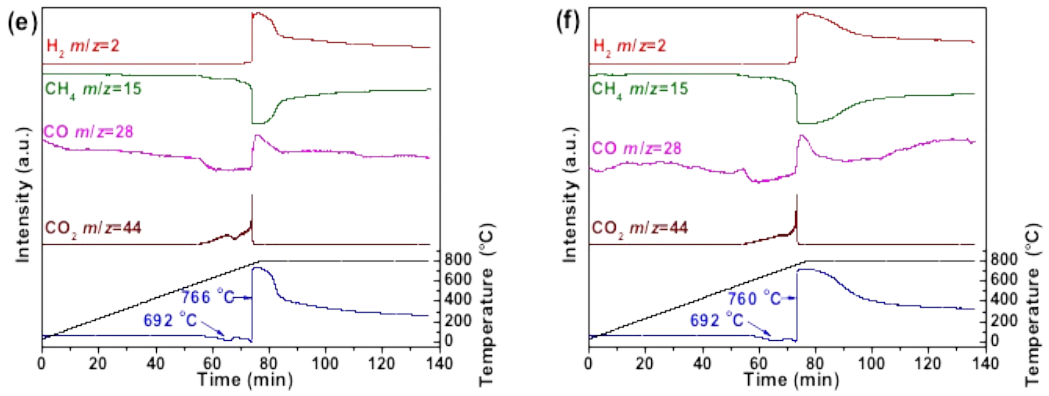


**Figure 8** $CH_4$-TPR-MS profile of (a) fresh CCO, (b) fresh Pt/CCO, (c)~(f) air regenerated/decarbonated Pt /CCO after 1st, 8th, 10th and 20th cycle. The blue and black line in the bottom of each panel stands for evolution of TCD signal and temperature, respectively.

The $CH_4$ reduction of Pt/CCO was further probed by $CH_4$-TPR-MS to understand the promoting effect of Pt. As shown in Figure 8a, the surface $Co_3O_4$ is reduced first, evidenced by the small inverse peak located at 692 °C accompanied by the detection of $CO_2$ according to the MS signal. The low-$CH_4$-conversion period is then followed, as also observed in the $CH_4$ combustion step in the 1st cycle of the proposed 3-step process. As the temperature increased, a sharp rise of TCD signal is observed. It is a transition from complete $CH_4$ combustion to $CH_4$ partial oxidation and $CH_4$ pyrolysis, as evidenced by the change of $CH_4$, $H_2$ and the appearance of CO in the MS signal. Therefore, the phase transitions regarding CCO species can be interpreted as: [surface $Co_3O_4$ +bulk CCO (692 °C)]→[CoO+CaO+trace Co(692 °C~800 °C 23 min)]→[Co+CaO+C(800 °C 23~40 min)]. It should also be pointed out that the fresh Pt/CCO exhibits a sharper peak in the $CH_4$-TPR profile (Figure 8b) compared to CCO (Figure 8a), suggesting the reaction between Pt/CCO and $CH_4$ is faster, possibly due to the boosted $CH_4$ activation by the *in situ* generated Pt species. Similar behaviors can be observed over fresh and spent Pt/CCO, as depicted in Figure 8b-

f. Notably, the transition from complete combustion to partial oxidation took place at 800 °C for 23 min over the fresh Pt/CCO, while advanced to about 760 °C after the first cycle over the spent Pt/CCO. It is consistent with the shortened low-$CH_4$-coversion period after multiple cycles as depicted in Figure 4b. Combining these observations, we speculate that the doping of Pt might promote $CH_4$ conversion and Pt in the cycled Pt/CCO is possibly very different from Pt in the fresh Pt/CCO.

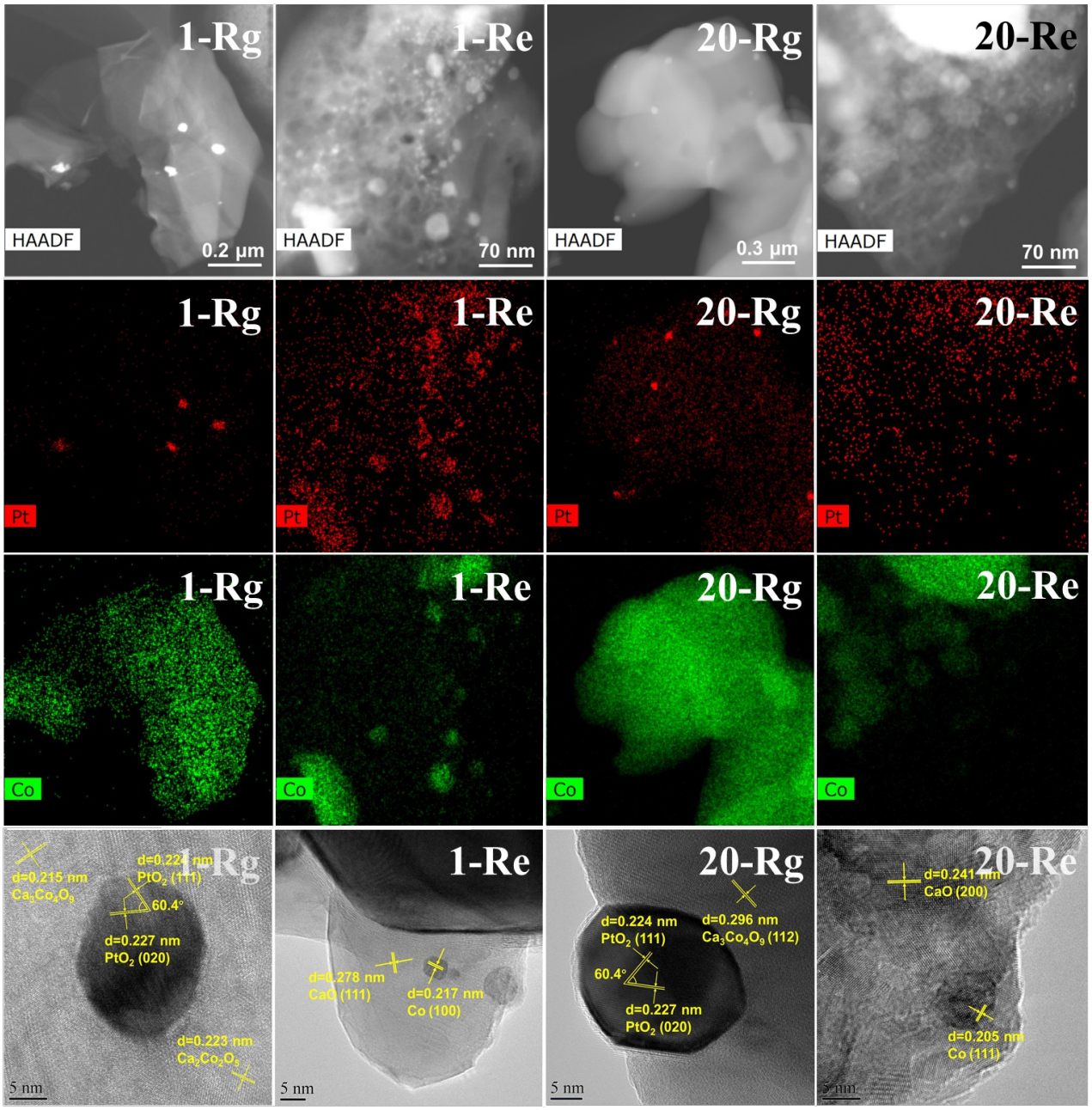

**Figure 9** Morphology and elemental distribution of Pt/CCO after air regeneration/decarbonation or $CH_4$ combustion step of the 1st and the 20th CLMC-SESRG-OC regeneration/sorbent decarbonation cycle. HAADF-STEM images, EDS element maps of Pt and Co, and HRTEM images are displayed from top to bottom panels successively. The number, 1 or 20, at the upper right corner of each panel stands for Pt/CCO used after 1st and 20th cycles, respectively. The letter "Rg" or "Re" stands for Pt/CCO used after OC regeneration/sorbent decarbonation step and $CH_4$ combustion step, respectively. Red and green color in the element maps stand for Pt and Co, respectively.

In order to verify our hypotheses, SEM and TEM were performed to understand the promoting effect under microscopic scale. As depicted in Figure S12, the hierarchical micro-structure with nanorods on the bulk plates could still be observed in the FESEM images of spent Pt/CCO materials, indicating that the promotion of Pt does not change the surface morphology.

As shown in Figure 9 and Figure S13, clear bright dots can be observed on the CCO flakes in HAADF-STEM images after the first CLMC-SESRG-OC regeneration/sorbent decarbonation cycle. They are identified as $PtO_2$ particles according to lattice fringes in the HRTEM images. Unlike the uniform distribution of Pt in the fresh Pt/CCO, $PtO_2$ particles ranging from 5 nm to 25 nm were formed during regenerating Pt/CCO in oxidative atmosphere. It is also worth mentioning that, apart from $PtO_2$ particles, the remaining Pt is homogenously dispersed with Co as the fresh Pt/CCO material does, indicating that the $PtO_2$ is probably from the agglomeration and oxidation of meta-stable Pt during the formation of CCO phases in the presence of $O_2$. It should be noted that a set of doublets located at *ca*. 77.5 eV and *ca*. 73.9 eV can be observed for air regenerated Pt/CCO cycled after both the 1st and the 20th cycle (Figure S14), corresponding to Pt(IV) species

consisting of both surface $PtO_2$ nanoparticles and substitution of Co by Pt in CCO lattices. The preservation of Pt(IV) species suggests the chemical states of Pt evolve in a highly reproducible manner throughout the 20 cycles, indicating the agglomeration of Pt is highly controllable. The newly formed surface $PtO_2$ may be crucial for boosting $CH_4$ conversion in the next $CH_4$ combustion step, probably due to the catalytic activity of Pt from the *in situ* reduction of $PtO_2$ and the surface $Pt^0$-$Pt^{4+}$ dipoles during the reduction, which may lower C-H bond energy, thereby promoting the activation of $CH_4$.[53]

Interestingly, after $CH_4$ combustion, the surface $PtO_2$ particles would be reduced and re-homogenized with metallic Co. As depicted in Figure 9, the $PtO_2$ particles become invisible and Pt is uniformly distributed with Co after $CH_4$ combustion. Moreover, the EDS line scanning profile and element maps of the particles formed after $CH_4$ combustion clearly show homogeneous dispersion of Co and Pt, as demonstrated by Figure S15. These results jointly suggest the formation of Pt-Co alloy [54], which is responsible for promoting $H_2$ production in the following SESRG step. Moreover, the signal of Pt could barely be detected by XPS (Figure S16), again indicating the formation of Pt-Co alloy rather than Pt-Co core-shell structure. The agglomeration and re-homogenization of Pt in the multifunctional material is highly repeatable during the 20 cycles as revealed by Figure 9 and Figure S13, demonstrating the structural stability of the multi-functional material proposed here.

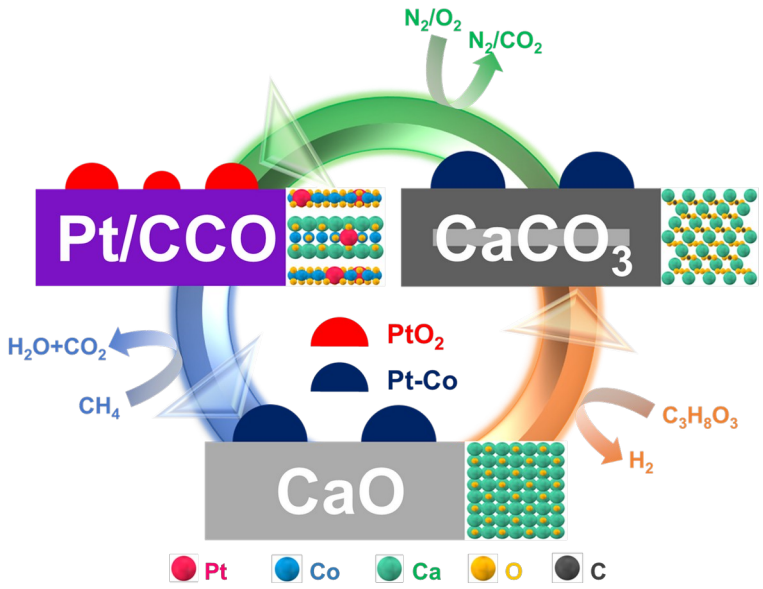


**Scheme 2** Illustration of the evolutions of Pt/CCO in the proposed CLMC-SESRG-OC regeneration/sorbent decarbonation cycle.

At this point, the evolutions of Pt/CCO multi-functional material can be concluded to rationalize the good and stable performance in the CLMC-SESRG coupling process, as illustrated in Scheme 2. After 1st cycle, $PtO_2$ particles are formed on the surface of CCO flake while the remaining Pt homogeneously disperses in the bulk CCO phase. During the combustion of $CH_4$ using the lattice oxygen as oxidant, the $PtO_2$ would be reduced to metallic Pt, accompanied by the reduction of bulk CCO phase to CaO and Co. After being completely reduced, metallic Pt can be homogenized with metallic Co possibly in the form of Pt-Co alloy. In the following SESRG step, CaO is gradually carbonated to $CaCO_3$. And then the following OC regeneration/sorbent decarbonation step under oxidative atmosphere merges CaO and cobalt oxides into each other's lattice to form CCO via a solid-state reaction [37]. Since Pt does not involve in the formation of CCO, it would be stripped off from metallic Co, resulting in the agglomeration on CCO surfaces and being oxidized to $PtO_2$. Thereafter, the $PtO_2$ further undergoes a solid-state reaction with

CCO, leading to the substitution of Co in CCO lattice [36]. At proper durations of regeneration period, the surface $PtO_2$ particles and homogeneous distribution of remaining Pt would be co-existed to facilitate the activation and conversion of methane.

# 4. CONCLUSIONS

In this work, energy-saving decarbonation and improved $H_2$ production from glycerol were achieved over a Pt/CCO multi-functional material with hierarchical micro-structures under the proposed 3-step CLMC-SESRG-OC regeneration/sorbent decarbonation scheme. The overall energy was 56% less than the conventional SESRG cycle using CaO as sorbent material, and the $H_2$ yield was 6.3 times higher than that of 2-step SESRG-sorbent decarbonation cycle using CCO material. It was demonstrated that 70% $CH_4$ conversion with over 90% $CO_2$ selectivity in terms of CLMC, and 120% $H_2$ yield with 96% purity in terms of SESRG can be achieved for 20 cycles. Furthermore, the highly reproduceable promoting effects of Pt towards $CH_4$ conversion and $H_2$ production were attributed to the formation of surface $PtO_2$ particles on the CCO flake as well as the homogeneous dispersion of remaining Pt in CCO phase and re-homogenization of Pt with Co to form Pt-Co alloy. Our results herein highlight the significance of process intensification and provide an innovative example of multi-functional materials for the combination of $H_2$ production and methane abatement.

# ACKNOWLEDGEMENTS

This work was supported by the National Natural Science Foundation of China (22078106), the Guangdong Natural Science Foundation (2017A030312005) and Science and Technology

Program of Guangzhou City (201707010058). We thank Ms. Dan Li, Dr. Shuoshi Liu and Prof. Siyu Yang for the help of overall energy balance calculation.

# REFERENCES


1. Dutta S. A review on production, storage of hydrogen and its utilization as an energy resource. *J. Ind. Eng. Chem.* 2014;20(4):1148-1156.
2. Luo M, Yi Y, Wang S, et al. Review of hydrogen production using chemical-looping technology. *Renewable Sustainable Energy Rev.* 2018;81:3186-3214.
3. Schwengber CA, Alves HJ, Schaffner RA, et al. Overview of glycerol reforming for hydrogen production. *Renewable Sustainable Energy Rev.* 2016, 58, 259-266.
4. Cui Y, Galvita V, Rihko-Struckmann L, Lorenz H, Sundmacher K. Steam reforming of glycerol: The experimental activity of $La_{1-x}Ce_xNiO_3$ catalyst in comparison to the thermodynamic reaction equilibrium. *Appl. Catal. B: Environ.* 2009;90(1-2):29-37.
5. He L, Parra JMS, Blekkan EA, Chen D. Towards efficient hydrogen production from glycerol by sorption enhanced steam reforming. *Energy Environ. Sci.* 2010;3(8):1046.
6. Iliuta I, Radfarnia HR, Iliuta, MC. Hydrogen production by sorption−enhanced steam glycerol reforming: sorption kinetics and reactor simulation. *AIChE J.* 2013;59:2105-2118.
7. Dang C, Wang H, Yu H, Peng F. Co-Cu-CaO catalysts for high-purity hydrogen from sorption-enhanced steam reforming of glycerol. *Appl. Catal. A: Gen*. 2017;533:9-16.
8. Shokrollahi Yancheshmeh M, Radfarnia HR, Iliuta MC. Sustainable production of high-purity hydrogen by sorption enhanced steam reforming of glycerol over $CeO_2$-promoted $Ca_9Al_6O_{18}$–CaO/NiO bifunctional material. *ACS Sustainable. Chem. Eng.* 2017;5(11):9774-9786.
9. Dou B, Zhang H, Cui G, et al. Hydrogen production by sorption-enhanced chemical looping steam reforming of ethanol in an alternating fixed-bed reactor: Sorbent to catalyst ratio dependencies. *Energy Convers. Manage.* 2018;155:243-252.

10. Bui M, Adjiman CS, Bardow A, et al. Carbon capture and storage (CCS): The way forward. *Energy Environ. Sci.* 2018; 11(5):1062-1176.
11. Fouad OA, Hassan AM, Abd El-Wahab H, Mohy Eldin A, Naser A-RM, Wahba OAG. Synthesis, characterization and application of some nanosized mixed metal oxides as high heat resistant pigments: $Ca_2CuO_3$, $Ca_3Co_2O_6$, and $NiSb_2O_6$. *J. Alloys Compd.* 2012;537:165-170.
12. Berastegui P, Eriksson SG, Hull S. A neutron diffraction study of the temperature dependence of $Ca_2Fe_2O_5$. *Mater. Res. Bull.* 1999;34(2):303-314.
13. Zhang YF, Zhang JX, Lu QM, Zhang QY. Synthesis and characterization of $Ca_3Co_4O_9$ nanoparticles by citrate sol-gel method. *Mater. Lett*. 2006;60:2443-2446.
14. Dang C, Li Y, Yusuf SM, et al. Calcium cobaltate: A phase-change catalyst for stable hydrogen production from bio-glycerol. *Energy Environ. Sci.* 2018;11(3):660-668.
15. Luo S, Zeng L, Fan L-S. Chemical looping technology: Oxygen carrier characteristics. *Annu. Rev. Chem. Biomol. Eng.* 2015;6:53-75.
16. Zeng L, Cheng Z, Fan JA, Fan L-S, Gong J. Metal oxide redox chemistry for chemical looping processes. *Nat. Rev. Chem*. 2018;2(11):349-364.
17. Schwach P, Pan X, Bao X. Direct conversion of methane to value-added chemicals over heterogeneous catalysts: challenges and prospects. *Chem. Rev.* 2017;117(13):8497-8520.
18. Kerr HR. Chapter 38 - Capture and separation technology gaps and priority research needs. In: Thomas DC. Carbon dioxide capture for storage in deep geologic formations. Amsterdam: Elsevier Science, 2005: 655-660.
19. Mattisson T, Lyngfelt A, Cho P. The use of iron oxide as an oxygen carrier in chemical-looping combustion of methane with inherent separation of $CO_2$. *Fuel* 2001;80(13):1953-

1962.

20. Scott SA, Dennis JS, Hayhurst AN, Brown T. In situ gasification of a solid fuel and $CO_2$ separation using chemical looping. *AIChE J*. 2006;52:3325-3328.
21. Adanez J, Abad A, Garcia-Labiano F, Gayan P, de Diego LF. Progress in chemical-looping combustion and reforming technologies. *Prog. Energy Combust. Sci.* 2012;38(2):215-282.
22. Fan L−S, Zeng L, Luo S. Chemical−looping technology platform. *AIChE J*. 2015;61:2-22.
23. MacDowell N, Florin N, Buchard A, et al. An Overview of $CO_2$ Capture Technologies. *Energy Environ. Sci.* 2010;3(11):1645-1669.
24. Porosoff MD, Yan B, Chen JG. Catalytic reduction of $CO_2$ by $H_2$ for synthesis of CO, methanol and hydrocarbons: challenges and opportunities. *Energy Environ. Sci.* 2016;9(1):62-73.
25. Abanades JC, Murillo R, Fernandez JR, Grasa G, Martinez I. New $CO_2$ capture process for hydrogen production combining Ca and Cu chemical loops. *Environ. Sci. Technol.* 2010;44(17):6901-6904.
26. Manovic V, Anthony EJ. Integration of calcium and chemical looping combustion using composite CaO/CuO-based materials. *Environ. Sci. Technol.* 2011;45(24),10750-10756.
27. Kierzkowska AM, Müller CR. Development of calcium-based, copper-functionalised $CO_2$ sorbents to integrate chemical looping combustion into calcium looping. *Energy Environ. Sci.* 2012;5(3):6061.
28. Fermoso J, Gil MV, Rubiera F, Chen D. Multifunctional Pd/Ni-Co catalyst for hydrogen production by chemical looping coupled with steam reforming of acetic acid. *ChemSusChem.* 2014;7(11):3063-3077.
29. Tang W, Hu Z, Wang M, Stucky GD, Metiu H, McFarland EW. Methane complete and partial

oxidation catalyzed by Pt-Doped $CeO_2$. *J. Catal.* 2010;273(2):125-137.

30. Torimoto M, Ogo S, Harjowinoto D, et al. Enhanced methane activation on diluted metal-metal ensembles under an electric field: Breakthrough in alloy catalysis. *Chem. Commun*. 2019;55(47):6693-6695.
31. Cheah SK, Massin L, Aouine M, Steil MC, Fouletier J, Gélin P. Methane steam reforming in water deficient conditions on $Ir/Ce_{0.9}Gd_{0.1}O_{2-x}$ catalyst: Metal-support interactions and catalytic activity enhancement. *Appl. Catal. B: Environ.* 2018;234:279-289.
32. Simakov DSA, Román−Leshkov Y. Highly efficient methane reforming over a low−loading $Ru/\gamma-Al_2O_3$ catalyst in a Pd−Ag membrane reactor. *AIChE J.* 2018;64: 3101-3108.
33. Xi Y, Heyden A. Direct oxidation of methane to methanol enabled by electronic atomic monolayer–metal support interaction. *ACS Catal.* 2019;9(7):6073-6079.
34. Zarei Senseni A, Rezaei M, Meshkani F. Glycerol steam reforming over noble metal nanocatalysts. *Chem. Eng. Res. Des.* 2017;123:360-366.
35. Silva JM, Ribeiro LS, Órfão JJM, Tosti S, Soria MA, Madeira LM. From sorption-enhanced reactor to sorption-enhanced membrane reactor: A step towards $H_2$ production optimization through glycerol steam reforming. *Chem. Eng. J.* 2019;368:795-811.
36. Huang Y, Zhao B, Lin S, Ang R, Sun Y. Structure and transport properties in $Ca_3Co_{4-X}M_xO_9$ (M=Re And Pt) ceramics. *Ceram. Int.* 2014;40(7):10545-10550.
37. Masset AC, Michel C, Maignan A, et al. Misfit-layered cobaltite with an anisotropic giant magnetoresistance:$Ca_3Co_4O_9$. *Phys. Rev. B.* 2000;62(1):166-175.
38. Itahara H, Seo WS, Lee S, Nozaki H, Tani T, Koumoto K. The formation mechanism of a textured ceramic of thermoelectric $[Ca_2CoO_3](0.62)[CoO_2]$ on Beta-$Co(OH)_2$ templates through in situ topotactic conversion. *J. Am. Chem. Soc.* 2005;127(17):6367-6373.

39. Cai QX, Wang J−G, Wang Y−G, Mei D. Mechanistic insights into the structure−dependent selectivity of catalytic furfural conversion on platinum catalysts. *AIChE J.* 2015;61:3812-3824.

40. Singh N, Lee M-S, Akhade SA, et al. Impact of pH on aqueous-phase phenol hydrogenation catalyzed by carbon-supported Pt and Rh. *ACS Catal*. 2019;9(2):1120-1128.

41. Lin X, Bao H, Zheng D, et al. An efficient family of misfit−layered calcium cobalt oxide catalyst for oxygen evolution reaction. *Adv. Mater. Interfaces.* 2018;5(23):1801281.

42. Ono LK, Yuan B, Heinrich H, Cuenya BR. Formation and thermal stability of platinum oxides on size-selected platinum nanoparticles: support effects. *J. Phys. Chem. C.* 2010;114(50): 22119-22133.

43. Tian ZQ, Jiang SP, Liang YM, Shen PK. Synthesis and characterization of platinum catalysts on multiwalled carbon nanotubes by intermittent microwave irradiation for fuel cell applications. *J. Phys. Chem. B.* 2006;110 (11):5343-50.

44. Martavaltzi CS, Lemonidou AA. Hydrogen production via sorption enhanced reforming of methane: development of a novel hybrid material—reforming catalyst and $CO_2$ sorbent. *Chem. Eng. Sci.* 2010;65(14):4134-4140.

45. Fernandez JR, Abanades JC, Grasa G. Modeling of sorption enhanced steam methane reforming—Part II: simulation within a novel Ca/Cu chemical loop process for hydrogen production. *Chem. Eng. Sci.* 2012; 84: 12-20.

46. Dewoolkar KD, Vaidya PD. Sorption-enhanced steam reforming of glycerol over Ni-hydrotalcite: effect of promotion with Pt. *ChemCatChem.* 2016;8(22):3499-3509.

47. Jiang B, Dou B, Wang K, et al. Sorption enhanced steam reforming of biodiesel by-product

glycerol on Ni-CaO-MMT multifunctional catalysts. *Chem. Eng. J.* 2017;313:207-216.

48. Asikin-Mijan N, Lee HV, Taufiq-Yap YH. Synthesis and catalytic activity of hydration–dehydration treated clamshell derived CaO for biodiesel production. *Chem. Eng. Res. Des.* 2015;102:368-377.
49. Chen X, Yang L, Zhou Z, Cheng Z. Core-shell structured CaO-$Ca_9Al_6O_{18}$@$Ca_5Al_6O_{14}$/Ni bifunctional material for sorption-enhanced steam methane reforming. *Chem. Eng. Sci.* 2017; 163: 114-122.
50. Zamboni I, Courson C, Kiennemann A. Fe-Ca interactions in Fe-based/CaO catalyst/sorbent for $CO_2$ sorption and hydrogen production from toluene steam reforming. *Appl. Catal. B: Environ*. 2017; 203: 154-165.
51. Courson C, Gallucci K. Chapter 3 - CaO-based high-temperature $CO_2$ Sorbents. In: Wang Q. Pre-combustion carbon dioxide capture materials. Cambridge: Royal Society of Chemistry, 2018: 144-237.
52. Guo J, Lou H, Zheng X. The deposition of coke from methane on a Ni/$MgAl_2O_4$ catalyst. *Carbon.* 2007;45(6):1314-1321.
53. Corro G, Torralba R, Pal U, Olivares-Xometl O, Fierro JLG. Total oxidation of methane over Pt/$Cr_2O_3$ catalyst at low temperature: Effect of $Pt^0$–$Pt^{x+}$ dipoles at the metal–support interface. *J. Phys. Chem. C* 2019;123(5):2882-2893.
54. Xie Z, Yan B, Kattel S, et al. Dry reforming of methane over $CeO_2$-Supported Pt-Co catalysts with enhanced activity. *Appl. Catal. B: Environ*. 2018;236:280-293.